# Detectability of the Warm/Hot Intergalactic Medium Through Emission Lines of OVII and OVIII

Kohji YOSHIKAWA[1,2], Noriko Y. YAMASAKI[3], Yasushi SUTO[1,2],

Takaya OHASHI[4], Kazuhisa MITSUDA[3], Yuzuru TAWARA[5], and Akihiro FURUZAWA[5]

[1]*Research Center for the Early Universe (RESCEU), School of Science,*

*University of Tokyo, Tokyo 113-0033*

*kohji@utap.phys.s.u-tokyo.ac.jp*

[2]*Department of Physics, School of Science, University of Tokyo, Tokyo 113-0033*

[3]*The Institute of Space and Astronautical Science (ISAS),*

*3-1-1 Yoshinodai, Sagamihara, Kanagawa 229-8510*

[4]*Department of Physics, Tokyo Metropolitan University, 1-1 Minami-Osawa, Hachioji, Tokyo 192-0397*

[5]*Department of Physics, Nagoya University, Furo-cho, Chikusa-ku, Nagoya 464-8602*

## Abstract

Most of cosmic baryons predicted by the big-bang nucleosynthesis has evaded the direct detection. Recent numerical simulations indicate that approximately 30 to 50 percent of the total baryons in the present universe is supposed to take a form of warm/hot intergalactic medium (WHIM) whose X-ray continuum emission is very weak. To identify those missing baryons, we consider in detail the detectability of WHIM directly through emission lines of OVII (561, 568, 574, 665eV) and OVIII (653eV). For this purpose, we create mock spectra of the emission lines of WHIM using a light-cone output of cosmological hydrodynamic simulations. While the predicted fluxes are generally below the current detection limit, an unambiguous detection will be feasible with a dedicated X-ray satellite mission that we also discuss in detail. Our proposed mission is especially sensitive to the WHIM with gas temperature $T = 10^{6-7}$K and overdensity $\delta = 10 - 100$ up to a redshift of 0.3 without being significantly contaminated by the cosmic X-ray background and the Galactic emissions. Thus such a mission provides a unique and important tool to identify a large fraction of otherwise elusive baryons in the universe.

**Key words:** cosmology: miscellaneous — X-rays: general — methods: numerical

## 1. Introduction

*Missing mass* or dark matter in the universe has been well recognized as one of the central problems both in observational cosmology and in astro-particle physics for more than 20 years. Nevertheless the nature of dark matter is hardly understood yet. *Missing baryons*, on the other hand, do not seem to have attracted much attention until very recently despite the fact that baryons are clearly the best understood component in the universe. Fukugita, Hogan, & Peebles (1998) are one of the first who explicitly pointed out the importance of studying the missing baryons, or *the cosmic baryon budget*. Subsequent numerical simulations (e.g., Cen & Ostriker 1999a; Davé et al. 2001) indeed suggest that approximately 30 to 50 percent of total baryons at $z = 0$ take the form of the warm-hot intergalactic medium (WHIM) with $10^5 \mathrm{K} < T < 10^7 \mathrm{K}$ which has evaded any direct detection so far. Unfortunately WHIM does not exhibit strong observational signature, and its detection has been proposed only either through the OVI absorption features in the QSO spectra (Hellsten, Gnedin, Miralda-Escude 1998; Perna & Loeb 1998; Fang & Canizares 2000; Cen et al. 2001; Fang & Bryan 2001; Fang, Bryan, Canizares 2002) or the possible contribution to the cosmic X-ray background in the soft band (Croft et al. 2001; Phillips, Ostriker, & Cen 2001).

Tripp, Savage & Jenkins (2000) and Tripp (2001) reported the first detection of the WHIM at low redshifts ($z \simeq 0.2$) through the OVI absorption lines in the spectra of a bright QSO H1821+643 observed by *FUSE* satellite, and they found that the absorbers are collisionally ionized with the metallicity $Z > 0.1 Z_\odot$ and have the number density $dN/dz \simeq 50$. Using *Chandra* observatory, Nicastro et al. (2002) and Fang et al. (2002) also detected the absorption lines of OVII, OVIII and NeIX at $z < 0.1$ in the spectrum of PKS 2155-304. Their spectral analyses indicate that the number density and temperature of the absorber are $n_e \simeq 6 \times 10^{-6}$ cm$^{-3}$ and $T = 5 \times 10^5$ K, respectively, with the coherent size being $\sim 3$ Mpc. This may be interpreted as WHIM in the nearby filamentary structures. Simcoe, Sargent, & Rauch (2002) observed the high redshift ($2.2 < z < 2.7$) OVI absorption line systems in several QSO spectra. Those are also interpreted as WHIM at high redshifts; the strong spatial clustering of the absorbers implies that they may indeed trace the large-scale structure in the universe.

In those attempts to detect WHIM through the absorption line systems, the observations are quite limited to particular lines-of-sight toward QSOs. The unbiased exploration of WHIM, however, requires a systematic survey-type observation, which motivates us to consider a possibility to identify emission line features of WHIM, in particular, those of OVII (561eV:1s$^2$–1s2s), OVII (568eV:1s$^2$–1s2p), OVII (574eV:1s$^2$–1s2p), OVII (665eV:1s$^2$–1s3p) and OVIII (653eV:1s–2p). The major obstacle against this attempt is the Galactic emission; our Galaxy harbors a significant amount of interstellar gas with similar temperature with WHIM, and the Galactic emission is typically two orders of magnitude stronger than the expected WHIM emission (McCammon et al. 2002). For instance, recently Kaastra et al. (2003) claimed

the detection of O$\textsc{vii}$ emission lines in the outskirts of galaxy clusters with *XMM–Newton*. Unfortunately because of the limited energy resolution ($\simeq 80$ eV) of the mission, it is not easy to distinguish the WHIM and the Galactic components in a convincing manner. This indicates the importance of the energy resolution of a detector for a reliable identification of WHIM. In fact, we show below that with an energy resolution of $\Delta E \sim 2$eV which is achievable in near future, one can distinguish the redshifted emission lines of O$\textsc{vii}$ and O$\textsc{viii}$ from other prominent Galactic lines.

The rest of the paper is organized as follows; section 2 summarizes the outline of our cosmological simulations and the model for metallicity evolution. Section 3 discusses the major noise sources and requirements for the instrument for the successful detection of oxygen emission lines. We present the predicted mock spectra assuming fiducial parameters for our proposed mission in section 4, and consider consider the detectability of the WHIM in section 5. Finally section 6 is devoted to implications and discussion of the present paper.

## 2.  Modeling Metallicity Evolution of Intergalactic Medium

### 2.1.  *Cosmological Hydrodynamic Simulation of Intergalactic Medium*

We use the simulation data of Yoshikawa et al. (2001), which are briefly described here. The simulation code is a hybrid of Particle–Particle–Particle–Mesh (PPPM) Poisson solver and smoothed particle hydrodynamics (SPH). We employ $128^3$ dark matter particles and the same number of gas particles within the periodic simulation cube of $L_{\mathrm{box}} = 75h^{-1}$Mpc per side. We adopt a spatially-flat $\Lambda$CDM universe with $\Omega_0 = 0.3$, $\Omega_{\mathrm{b}} = 0.015h^{-2}$, $\lambda_0 = 0.7$, $\sigma_8 = 1.0$, and $h = 0.7$, where $\Omega_0$ is the density parameter, $\Omega_{\mathrm{b}}$ is the baryon density parameter, $\lambda_0$ is the dimensionless cosmological constant, $\sigma_8$ is the rms density fluctuation top-hat smoothed over a scale of $8h^{-1}$Mpc, and $h$ is the Hubble constant in units of 100 km/s/Mpc. Thus the mass of each dark matter and gas particle is $2.4 \times 10^9 M_\odot$ and $2.2 \times 10^{10} M_\odot$, respectively. The initial condition is generated at redshift $z = 36$ and is evolved up to the present.

The ideal gas equation of state with an adiabatic index $\gamma = 5/3$ is adopted, and the effect of radiative cooling is incorporated using the cooling rate of Sutherland & Dopita (1993) adopting a metallicity [Fe/H]$= -0.5$ We also implement the cold gas decoupling technique for the phenomenological treatment of the multi-phase nature of baryons; we decouple radiatively cooled gas particles from the remaining gas particles and regard the former as stellar components in galaxies, which provides an approximate prescription of galaxy formation. The effects of energy feedback from supernovae and the UV background heating are ignored in our simulation.

All the cosmological observations are carried out over the past lightcone. In the present study, this is particularly important because we do not know *a priori* the redshifts of the corresponding WHIM along the line-of-sight. In order to properly model a realistic observation surveying a $5° \times 5°$ region, we create the lightcone data as schematically illustrated in Figure 1;

we first stack eleven simulation cubes at different redshifts sampled from $z = 0$ to $z = 0.3$. The size of the survey area corresponds to the simulation boxsize at $z = 0.3$; $d_\mathrm{A}(z = 0.3) \times 5° \approx L_\mathrm{box}/(1 + 0.3)$ where $d_\mathrm{A}(z)$ is the angular diameter distance toward a redshift $z$. Specifically we use data at $z = 0$, 0, 0.047, 0.047, 0.096, 0.096, 0.148, 0.148, 0.202, 0.202, and 0.259 (due to the limited number of outputs, we sometimes have to use data at the same redshift twice). In order to avoid the artificial coherent structure along the line of sight, we randomly choose a position in the cube and periodize the particle positions, and also randomly exchange the $x$-, $y$- and $z$-axes in constructing the light-cone output.

## 2.2. Metallicity of the intergalactic medium

Since the resolution of our cosmological simulations is insufficient to trace the metallicity evolution, we have to adopt an ad-hoc model for the chemical evolution of the intergalactic medium (IGM). Oxygens that we are interested in here are mainly produced via Type II supernovae in galaxies, and are generally believed to be ejected into intergalactic space via the supernova-driven galactic wind and/or other dynamical processes like mergers and tidal interaction of two galaxies (e.g., Gnedin & Ostriker 1997; Nath & Trenthanm 1997; Gnedin 1998; Cen & Ostriker 1999a; Cen & Ostriker 1999b; Ferrara, Pettini, & Shchekinov 2000). For definiteness, we consider the following four possibilities in order to bracket the plausible range of observational and theoretical uncertainties.

**model I:** the metallicity is set to be $Z = 0.2 Z_\odot$ independently of redshifts and the densities of the IGM.

**model II:** the metallicity is assumed to be spatially uniform but increase in proportion to the cosmic time $t$:

$$Z = 0.2 (t/t_0) Z_\odot, \tag{1}$$

where $t_0$ is the age of the universe.

**model III:** the metallicity is assumed to be correlated with the local IGM density $\rho_\mathrm{IGM}(\mathbf{x}, t)$ relative to the mean baryon density of the universe $\bar{\rho}_\mathrm{b}(t)$. To be specific, we adopt

$$Z = 0.005 (\rho_\mathrm{IGM}/\bar{\rho}_\mathrm{b})^{0.33} Z_\odot \tag{2}$$

from our fit to the metallicity–density relation at $z = 0$ of the galactic wind driven metal ejection model of Aguirre et al. (2001b).

**model IV:** we assume the similar gas density dependence of the metallicity as model III but use the fit to the radiation pressure ejection model of Aguirre et al. (2001b) where the stellar light exerts radiation pressure on the interstellar dust grains and expels them into the hosting galactic halos and the ambient IGM. Actually, we find that the results of Aguirre et al. (2001b) in this model have the density dependence of the metal distribution similar to that of model III except for the overall normalization:

$$Z = 0.02 (\rho_\mathrm{IGM}/\bar{\rho}_\mathrm{b})^{0.3} Z_\odot. \tag{3}$$

Note that Aguirre et al. (2001b) concluded that only the radiation pressure ejection model (model IV) reproduces the typical metallicity in intracluster medium, while the observed metallicity of Lyman-$\alpha$ clouds at $z \approx 2-3$ may be accounted for by both models III and IV.

## 3.   Contaminating Sources and Requirements for the Instruments

In this section, we discuss the contaminating sources in detecting the emission lines of WHIM and the requirements for the detector and the telescope to evade such contaminations.

The major contaminating sources are the cosmic X-ray background (CXB) and the emission lines of hot gas which resides in the Galactic halo. According to McCammon et al. (2002), Nvii (500eV) and Cvi (368eV) are the other prominent lines in the Galactic emission below oxygen line energies. The Oviii line of WHIM at $z < 0.3$ that we consider here is free from the confusion with the above two lines, and thus we focus on the energy range between 500eV and 700eV.

Thus the detection threshold in this energy range is basically determined by the intensity of the CXB. Miyaji et al. (1998) suggested that the absolute intensity of the CXB below 1 keV has a systematic error of 20–30 % in comparison with the *ROSAT* and *ASCA* measurements. Strictly speaking, however, the soft component of the "CXB" is supposed to be dominated by the Galactic diffuse emission. Kushino et al. (2002) found that the *ASCA* GIS diffuse background spectrum after removing the point source contributions consists of a hard power-law component and a soft component. More importantly they found that the intensity of the soft component varies significantly from field to field (its $1\sigma$ fractional variation amounts to $52^{+4}_{-5}\%$ of the average CXB intensity), and indeed becomes stronger toward the Galactic Center; the spatial distribution is well fitted with a finite disk model with a radius of $(1.15\pm0.23)R_g$, and a scale height of $(0.19\pm0.08)R_g$, where $R_g$ is the distance to the Galactic center. This implies that the soft component (below 1 keV) is dominated by the Galactic diffuse emission. They estimated the average flux of $6\times10^{-9}$ erg cm$^{-2}$s$^{-1}$sr$^{-1}$ between 0.5 and 0.7 keV by averaging 91 fields, corresponding to the flux density of $f_{\mathrm{B}} = 3 \times 10^{-8}$ erg cm$^{-2}$s$^{-1}$sr$^{-1}$keV$^{-1}$.

The primary requirement for the detector of the WHIM emissions is its high energy resolution to distinguish the Oxygen lines of WHIM at an intermediate redshift from their Galactic counterparts. The observational features of the Galactic emission lines are described in detail by McCammon et al. (2002). They observed $\sim 1$ sr sky centered at $l = 90°, b = 60°$ with a resolution of 9 eV, and found the line intensities of $4.8 \pm 0.8$ photons cm$^{-2}$s$^{-1}$sr$^{-1}$ ($4.4 \pm 0.7 \times 10^{-9}$ erg cm$^{-2}$s$^{-1}$ sr$^{-1}$ ) for the Ovii triplet and of $1.6 \pm 0.4$ photons cm$^{-2}$s$^{-1}$sr$^{-1}$ ($1.7 \pm 0.4 \times 10^{-9}$ erg cm$^{-2}$s$^{-1}$ sr$^{-1}$ ) for the 653 eV Oviii line. With a better energy resolution ($\Delta E < 6$ eV), the lines of $\delta z \sim 0.01$ can be separated from the Galactic components. In addition, the separation of Ovii triplets may lead to the estimation of the temperature of WHIM from their line ratios.

Another important requirement is the high efficiency of the throughput of the telescope. Since the emission lines of WHIM are generally weak, we need large $S_{\mathrm{eff}}\Omega$ for their successful detection, where $S_{\mathrm{eff}}$ is the effective area and $\Omega_{\mathrm{tot}}$ is the total field-of-view of detectors. To realize a large mirror with $S_{\mathrm{eff}}\Omega_{\mathrm{tot}} > 100\mathrm{cm}^2\mathrm{deg}^2$, we are currently pursuing the possibility of 4-stage X-ray telescopes (Furuzawa et al. 2003, in preparation). In contrast to the standard 2-stage X-ray mirrors, 4-stage telescopes will be able to achieve a shorter focal length and a wider field-of-view. The short focal length makes it possible to construct a smaller detector with the same field-of-view. This is essential for the X-ray micro-calorimeters to simultaneously achieve a small heat capacitance and a good energy resolution. We simulated a nested 4-stage telescope with a diameter of 60 cm and a focal length of 70 cm by a ray-tracing program, and found that the throughput at 0.7 keV is $S_{\mathrm{eff}}\Omega_{\mathrm{tot}} = 220\eta$ $\mathrm{cm}^2\mathrm{deg}^2$ with $\eta$ being the overall efficiency of the detector (Furuzawa et al. 2003, in preparation).

Consider a detector with the effective area $S_{\mathrm{eff}}$, the field-of-view $\Omega$, and the energy resolution $\Delta E$ at the line energy $E$. Then the signal-to-noise ratio of emission lines is written as

$$
(S/N)^2 = \frac{\left(\dfrac{\bar{f}_{\mathrm{em}}S_{\mathrm{eff}}\Omega T_{\mathrm{exp}}}{E}\right)^2}{\left(\dfrac{f_{\mathrm{B}}\Delta E S_{\mathrm{eff}}\Omega T_{\mathrm{exp}}}{E}\right) + \left(\dfrac{\bar{f}_{\mathrm{em}}S_{\mathrm{eff}}\Omega T_{\mathrm{exp}}}{E}\right)}
$$
$$
= \frac{\bar{f}_{\mathrm{em}}^2 S_{\mathrm{eff}}\Omega T_{\mathrm{exp}}}{(f_{\mathrm{B}}\Delta E + \bar{f}_{\mathrm{em}})E}, \tag{4}
$$

where $\bar{f}_{\mathrm{em}}$ is the flux of emission lines averaged over the given size of pixels on the detector, and $T_{\mathrm{exp}}$ is the exposure time. The denominator in the above expression indicates the noise level contributed from the CXB and the Poisson noise of emission from WHIM in terms of the corresponding number of photons. Figure 5 shows the signal-to-noise ratio of OVIII 653 eV emission lines for various values of $S_{\mathrm{eff}}\Omega T_{\mathrm{exp}}$ as a function of a flux of the lines, where we adopt $\Delta E = 2\mathrm{eV}$ as a nominal energy resolution of our fiducial detector. This indicates that in the case of $S_{\mathrm{eff}}\Omega T_{\mathrm{exp}} = 10^7$ $\mathrm{cm}^2$ $\mathrm{deg}^2$ sec and $10^8$ $\mathrm{cm}^2$ $\mathrm{deg}^2$ sec, one can detect emission lines with fluxes greater than $7 \times 10^{-11}$ erg $\mathrm{cm}^{-2}$ $\mathrm{sec}^{-1}$ $\mathrm{sr}^{-1}$ and $1.5 \times 10^{-11}$ erg $\mathrm{cm}^{-2}$ $\mathrm{sec}^{-1}$ $\mathrm{sr}^{-1}$ with sufficient ($S/N > 10$) statistical significance, respectively.

Actually, the emission from hot intra-cluster medium (ICM) in galaxy clusters can be also an important contaminating source. For the central regions of galaxy clusters, the emission from ICM is predominant, and thus the identification of OVII and OVIII lines becomes difficult at directions toward such regions. Therefore, the detection limit inferred from Equation (4) may be interpreted as a lower limit. This contamination, however, is important only in central regions of galaxy clusters. Actually, as we will see below, the emission lines above the detection threshold inferred from Equation (4) generally produce detectable spectral signatures.

Considering the transmission of the entrance window and the quantum efficiency of the

detector, a realistic value of $\eta$ may be $\sim 0.5$. In what follows, therefore, we assume the detector throughput of $S_{\mathrm{eff}}\Omega_{\mathrm{tot}} = 100$ cm$^2$ deg$^2$, and the spectroscopic energy resolution of $\Delta E = 2$ eV. The field-of-view $\Omega$ may be chosen somewhere in a range of $0.5°$ to $1°$, and is filled with a detector array of $32 \times 32$ pixels. This specification is compared with the on-going/planned X-ray missions in Table 1, where the expected sensitivities for the emission lines of current and proposed X-ray satellite missions are summarized. The first two are the current working missions; *Chandra* (Weisskopf et al. 2000) has a good spatial resolution of $1''.5$ (FWHM) and *XMM-Newton* (Strüdel et al. 2001) has a large effective area of 1200 cm$^2$. While *Chandra* has the transmission grating spectrometers HETG and LETG, and *XMM-Newton* has the reflection grating spectrometer, RGS, the energy resolution of those grating instruments for diffuse emission lines is worse than those of X-ray CCDs. Table 1 lists the sensitivities of X-ray CCD detectors, ACIS-S3 for *Chandra* and EPIC-pn for *XMM-Newton*. Astro-E II (http://www.astro.isas.ac.jp/astroe) is a Japan-USA mission which will be launched in 2005. The XRS detector will be the first X-ray micro-calorimeter in orbit and have an energy resolution of 6 eV. Due to the small effective area and the field-of-view, however, the sensitivity of the XRS is worse than that of XIS consisting of four X-ray CCDs. The *Constellation-X* (http://constellation.gsfc.nasa.gov) is a US mission of high throughput consisting of four space-crafts. The flux limit is estimated on the basis of the current design of SXT and TES (transition-edge sensor) calorimeters with 2 eV energy resolution. The *XEUS* (http://astro.estec.esa.nl/XEUS/) will have a huge X-ray mirror of 6 m$^2$ and TES calorimeters. Since those missions are all designed as X-ray observatories for general purposes, both a large effective area and a good spatial resolution are preferred and the field-of-view has to be necessarily smaller. On the other hand, the nested 4-stage telescope that we propose here is feasible even with a small satellite, and still the sensitivity for the diffuse X-ray line emission exceeds those of the larger missions. In this sense, it has important and complementary advantages over other current/future X-ray missions.

## 4. Mock Observation of Oxygen Emission Lines from the Simulated Warm/Hot IGM

### 4.1. Calculation of O VII and O VIII Emission

We divide the entire lightcone data, which we describe in section 2, into $64 \times 64$ square grids on the celestial plane and 128 grids equally spaced along the redshift direction (see Fig. 1). Thus we have $64 \times 64 \times 128$ cells in total. For the $J$-th cell, we compute the surface brightness $S_J$ due to the emission lines of O VII and O VIII as

$$S_J = \sum_i \frac{\rho_i m_i}{4\pi(1+z_i)^4 \Delta A_i} \left(\frac{X}{m_{\mathrm{p}}}\right)^2 f_{\mathrm{e},i}^2 \epsilon(T_i, Z_i), \tag{5}$$

$$\Delta A_i \equiv d_{\mathrm{A}}^2(z_i)\Delta\omega, \tag{6}$$

where the summation is over the gas particles (labelled $i$) within the $J$-th cell. In the above

7

expression, $X$ is the hydrogen mass fraction (we adopt 0.755), $m_{\mathrm{p}}$ is the proton mass, $\epsilon(T, Z)$ is the oxygen line emissivities in units of the power input normalized to the electron densities as defined by Mewe, Gronenschild, & van den Oord (1985), $\Delta\omega = (5°/64)^2$ is the solid angle of each cell, and $f_{\mathrm{e},i}$, $z_i$, $\rho_i$, and $m_i$ denote the electron number fraction relative to the hydrogen, redshift, mass density and mass of the $i$-th gas particle, respectively.

In the present study, we assume the collisional ionization equilibrium in computing $f_{\mathrm{e}}$ and $\epsilon$. Strictly speaking, however, this assumption may not be completely valid in most regions of the WHIM. Adopting the typical WHIM parameters ($n_{\mathrm{e}} = 1 \times 10^{-5}$ cm$^{-3}$ and $T = 10^6$K), for instance, the recombination timescale of HII $\simeq 3 \times 10^{11}$ yr significantly exceeds that of of the collisional ionization ($\simeq 10^5$ yr). Nevertheless we adopt the collisional ionization equilibrium for simplicity as in the case of all the previous simulation studies of the absorption lines due to the WHIM. We plan to discuss the non-equilibrium effect elsewhere.

Figure 2 shows the emissivities of OVII and OVIII lines as a function of gas temperature, where we set the metallicity as $Z = Z_\odot$, from the table in the SPEX ver 1.10 (http://www.rhea.sron.nl/divisions/hea/spex). The intensity of OVII emission lines, a triplet of 574 eV, 581 eV and 588 eV, is peaked around at $T = 2 \times 10^6$ K, and the OVIII 653 eV line becomes dominant at $T > 3 \times 10^6$ K.

Figure 3 shows the total intensity maps of OVII and OVIII emission lines of WHIM (*left panels*) and the bolometric X-ray emission (*right panels*) integrated over the redshift range of $0 < z < 0.3$ (*upper panels*), $0.03 < z < 0.04$ (*middle panels*), $0.09 < z < 0.11$ (*lower panels*). The six squares labelled A to F indicate the regions whose mock spectra will be presented in the next section.

## 4.2. Calculation of Simulated Soft X-Ray Spectra

For each of $64 \times 64$ cells on the celestial plane, we also compute the spectrum of WHIM and/or ICM at soft X-ray energy band ranging from 450eV to 700eV. The flux intensity at an energy range from $E$ to $E + \Delta E$ can be calculated as a superposition of spectra for SPH particles by

$$
\begin{aligned}
F(E, E + \Delta E) = \sum_i \frac{\rho_i m_i}{4\pi(1+z_i)^4 \Delta A_i} \left(\frac{X}{m_{\mathrm{p}}}\right)^2 f_{\mathrm{e},i}^2 \\
\times \int_{E(1+z_i)}^{(E+\Delta E)(1+z_i)} P(E', T_i, Z_i) dE',
\end{aligned} \tag{7}
$$

where the summation is over the SPH particles and $P(E, T, Z)$ is the template spectrum for temperature $T$ and metallicity $Z$. The set of template spectra $P(E, T, Z)$ is created using SPEX software package and is tabulated for temperature range $10^5$K $< T < 10^8$K and metallicity range $10^{-3} Z_\odot < Z < Z_\odot$. Here, we assume again that all the baryons are under collisional ionization equilibrium in this temperature range. Figure 4 shows the template spectra of collisionally ionized plasma with temperature $T = 10^6$ K, $10^{6.5}$ K, and $10^7$ K, and with metallicity $Z = Z_\odot$

and $Z = 0.1Z_{\odot}$. At a lower temperature, $T = 10^6$ K, we have strong emission lines of the Ovii triplets ($E = 561, 568, 574$ eV). On the other hand, at $T = 10^{6.5}$ K and $10^7$ K, Oviii line at $E = 653$ eV and many Fexvii lines at $E > 700$ eV emerge.

Using the template spectra (Fig. 4) and the proposed detector specification, we construct mock emission spectra of WHIM over the lightcone data as follows. First we compute the total photon numbers on each $(5°/64)^2$ grid due to the three components; the WHIM emission spectra according to Equation (7), the CXB contribution adopting $f_{\mathrm{CXB}} = 6 \times 10^{-9}$ erg cm$^{-2}$s$^{-1}$sr$^{-1}$ between 0.5 and 0.7 keV and a photon index $\Gamma = 6$ (Kushino et al. 2002), and the Galactic emission lines of Oxygen and Nitrogen as observed by McCammon et al. (2002). In practice, we compute the numbers of photon per each spectroscopic bin assuming a given exposure time. Then we assign the additional photon number fluctuations per each bin according to the corresponding Poisson statistics. The energy spectrum of photons is convolved with the response function of a detector which we approximate by a Gaussian with a FWHM of 2eV.

The upper panel of Figure 6 shows an example of the simulated composite spectrum, which includes the contribution from WHIM, CXB, the Galactic emission lines, with exposure time $T_{\mathrm{exp}} = 3 \times 10^5$ sec for the region A (0.88 deg$^2$) in Fig. 3. Strong lines in the upper panel correspond to the Galactic emission lines of Nvii at 498 eV, Ovii at 561eV, 568 eV, 574 eV, and 665 eV, and Oviii at 653 eV. Clearly the separation of the Galactic component from the WHIM emission lines is the most essential. In order to mimic the realistic separation procedure, we construct an independent realization of spectra which consists purely of the CXB and Galactic emission lines but using the different sets of random numbers in adding the Poisson fluctuations in each bin. Then the latter spectra are subtracted from the mock spectra (WHIM + CXB and Galactic emissions), which yields a residual mock spectrum purely for the WHIM (*dots with Poisson error bars in lower panel*). For comparison, we plot the noiseless WHIM spectrum from simulation in solid line. The emission lines with labels in the lower panel indicate Oviii and Ovii triplet lines whose surface brightness exceeds our nominal limiting flux (see the top-right panel of Figure 7). The Oviii emission lines from the WHIM at $z = 0.04 - 0.23$ can be indeed observed as the residual prominent emission lines between $E = 500 - 630$ eV, though they are also contaminated by other emission lines. Thus this plot indicates that the emission lines exceeding the residual photon number $\sim 100$ counts/bin are detectable with a three-day exposure.

In reality, the continuum spectra from CXB, Galactic diffuse, and WHIM would be hard to be separated. As indicated in the above idealistic example, however, the continuum level of the WHIM emission is just within the fluctuation of the CXB and the Galactic emission. Thus the uncertainty of the continuum level does not affect the identification of the emission lines using the proper line fitting procedure.

The absorption due to the interstellar medium of the Galaxy is another possible source for systematic errors in detecting the WHIM emission. At a photon energy of $E = 0.6$keV,

the dominant absorption is due to the Galactic oxygen as well as other metals. The oxygen abundance is usually assumed to be in proportion to the Galactic neutral hydrogen. So one can use the observed column density of neutral hydrogen $N_{\rm H}$ in inferring the degree of the absorption. Figure 1 of (Morrison & McCammon 1983) indicates that the absorption cross section around $E = 0.6$keV is $\sigma \approx 7.4 \times 10^{-22}$cm$^2$ for 1 solar metallicity. So the regions of the sky with $N_{\rm H} = 3 \times 10^{20}$ cm$^{-2}$ and $10^{20}$ cm$^{-2}$ decrease the soft X-ray intensity around $E = 0.6$keV by 20% and 7%, respectively. In other words, if we preferentially select survey fields with $N_{\rm H} < 10^{20}$ cm$^{-2}$, the absorption is less than 10%. Therefore even taking account of the uncertainty of the metal abundance and $N_{\rm H}$, we expect that the absorption effect may be corrected within a few percent accuracy.

## 5.  Results

We illustrate results corresponding to two different types of observational strategies. One is a relatively shallow blank survey which attempts to detect the WHIM over the large fields in an unbiased manner. The other is a deeper survey which observes the pre-selected areas, for instance, the regions surrounding X-ray luminous clusters to search for the connecting filamentary WHIM from the clusters. The detector that we have roughly in mind here has an array of $32 \times 32$ pixels over the total field-of-view of $\Omega_{\rm tot} = (0.5 - 1.0)$ deg$^2$, which has a better angular resolution than that of our simulation grids ($5°/64 = 4.7$ arcmin). The higher angular resolution is in any case useful in removing the point sources, etc. In reality, however, a reasonably low detection threshold, i.e., $S_{\rm eff}\Omega T_{\rm exp} > 10^7$ cm$^2$ deg$^2$ sec discussed in the previous subsection, can be achieved only by merging many pixels at the expense of the angular resolution depending on the adopted value of $T_{\rm exp}$. Here, we assume that the total field-of-view is $\Omega_{\rm tot} = 0.88$ deg$^2$ which corresponds to $12 \times 12$ simulated grids.

With those in mind, we perform two simulated observations according to the above two strategies, respectively. The first adopts $T_{\rm exp} = 3 \times 10^5$ sec and combines the $12 \times 12$ simulated grids. Then the spatially resolved region corresponds to the the field-of-view of 0.88 deg$^2$, and $S_{\rm eff}\Omega T_{\rm exp} = 3 \times 10^7$ cm$^2$ deg$^2$ sec. The second adopts $T_{\rm exp} = 10^6$ sec and combines $4 \times 4$ grids. Thus each spatial resolution is now 0.098 deg$^2$, and $S_{\rm eff}\Omega T_{\rm exp} = 1.1 \times 10^7$ cm$^2$ deg$^2$ sec. As target regions, we select the square regions A, B and C in Figure 3 for the first strategy and D, E, and F for the second one. Since we expect that WHIM resides in the outskirts of galaxy clusters and/or in galaxy groups, it is quite natural to select vicinity of rich galaxy clusters as target regions. Actually, the regions that we select here turn out to contain a rich galaxy cluster at redshift $z = 0.04$ and several small galaxy groups at $0.09 < z < 0.011$ which cannot be probed by current typical X-ray observations. Various panels in Figure 3 are displayed to show the complementary nature of the X-ray thermal bremsstrahlung emission (right panels) and the oxygen emissions (left panels). Top panels correspond to the entire lightcone for $0 < z < 0.3$, and the middle and bottom panels illustrate the contribution from two regions at $0.03 < z < 0.04$

and $0.09 < z < 0.11$.

Consider first the shallow survey. Figure 7 shows the residual emission spectra (*left panels*) and the redshift profiles of gas overdensity, temperature, and Ovıı surface brightness (*right panels*) of the three regions A, B, and C assuming model I for metallicity. Labels in the left panels indicate the identification of emission lines in the corresponding redshift profiles in the right panels. Except for Ovıı 665eV emission lines which locate at $\simeq 10$eV blueward of prominent Ovııı lines, most of the emission lines without any labels are redshifted Fe xvıı lines. The dashed lines in the panels of Ovıı surface brightness indicate our detection limit $3 \times 10^{-11}$ erg s$^{-1}$ cm$^{-2}$ sr$^{-1}$ for $S/N = 10$ in the case of $S_{\mathrm{eff}} \Omega T_{\mathrm{exp}} = 3 \times 10^7$ cm$^2$ deg$^2$ sec. The filled histograms indicate those redshift bins ($\Delta z = 0.3/128$) whose surface brightness exceeds the above limiting flux. The region B encloses an X-ray cluster located at $z = 0.038$, and the region A contains a filamentary structure around the cluster, as is clearly shown in the *middle* panels of Figure 3. The region C lies close to, but is not directly associated with, the cluster. Rather it encloses poor groups of galaxies located at $z = 0.09 - 0.11$ (*lower* panels of Fig. 3), which are not visible in the X-ray thermal bremsstrahlung emission (see right panels of Fig. 3).

The spectra along the region B exhibit a strong Ovııı emission line at $E = 629$ eV, which originates from the intra-cluster medium of the X-ray cluster at $z = 0.038$ (Fig. 3). The Ovıı triplet emission lines around $E = 535 - 560$ eV are also ascribed to the same cluster. The region A sweeps the outer region of the cluster which is expected to contain less dense ($\delta \simeq 20$) but hotter ($T \simeq 1$ keV) IGM. In fact we do see a relatively mild Ovııı emission line at the cluster redshift. Finally in the region C we detect a strong Ovııı emission line at $E = 613$ eV and Ovıı triplet lines at $E = 525 - 540$ eV from a cluster at $z = 0.065$ as well as weaker emission lines at $E = 585 - 605$ eV from the galaxy groups at $z = 0.08 - 0.12$.

Turn to next the simulated deeper survey. Figure 8 is the same as Figure 7 but for the three regions D, E, and F. The detection limit for those plots is $6 \times 10^{-11}$ erg s$^{-1}$ cm$^{-2}$ sr$^{-1}$ for $S/N = 10$ in the case of $S_{\mathrm{eff}} \Omega T_{\mathrm{exp}} = 1.1 \times 10^7$ cm$^2$ deg$^2$ sec. The region D shows an emission line due to a substructure of a cluster at $z = 0.039$, and all the three regions exhibit the presence of galaxy groups at $z = 0.1 - 0.11$. The spectra in the regions D and E show the emission lines from the galaxy cluster and its substructure at $z = 0.039$. We note that the emission line in the region D corresponding to the $z = 0.039$ structure is stronger than the counterpart in the region E, although the temperature of the region D at $z = 0.039$ is $\simeq 7 \times 10^6$ K and in fact lower than that of the region E ($\simeq 2 \times 10^7$ K). This is because the emissivity of Ovııı decreases as the temperature exceeds $T \approx 3 \times 10^6$ K, and clearly demonstrates that the oxygen lines are more sensitive to the presence of the WHIM than that of the higher temperature gas associated with intra-cluster gas. The comparison of Figures 7 and 8 with Figure 3 indeed reveals that the WHIM that evades the detection in the X-ray is indeed detectable in its emission features in both shallow and deep surveys that we simulate here.

So far we show the results only for the metallicity model I. In order to show the de-

pendence on the assumption of metallicity, Figure 9 compares the spectra of the region D for the four metallicity models described in the last section. Since the emission lines in this region come from the WHIM at low redshifts, the metallicity evolution hardly changes their intensities. On the other hand, the model assumption on the density dependence significantly changes the result. Among the four models that we consider, model IV predicts the strongest emission lines, especially of Oviii at $E = 590$ eV and Ovii triplet at $E = 500 - 520$ eV, while the other three models predict very similar emission intensities. This is because model IV assumes the metallicity larger than $0.2Z_\odot$ for high density gas particles with $\rho > 10^3\bar{\rho}_{\rm b}$, which mainly reside in the intra-cluster medium. The emission lines from mildly dense regions including the Oviii line in $E = 630$ eV, on the other hand, are not sensitive to the metallicity model.

Figure 10 plots the distribution of temperatures and densities for all the 0.098 deg$^2$ regions over the entire survey of $5° \times 5°$. The different symbols indicate the range of surface brightness of emission lines for Oviii 653eV (*left panels*) and Ovii 561eV (*right panels*). Top to bottom panels correspond to the four different metallicity models. Note that the temperature and density of each region are estimated by smoothing over the fixed *angular* scale (0.098 deg$^2$), and therefore the corresponding physical smoothing lengths $R_s$ are different depending on the redshift of each region; $R_s = 1.6h^{-1}$Mpc, $3.1h^{-1}$Mpc and $4.6h^{-1}$Mpc at $z = 0.1$, 0.2 and 0.3, respectively. Therefore, the actual density is $\sim 10$ times higher than the smoothed density.

The Oviii emission lines from regions with $S > 6 \times 10^{-11}$ erg s$^{-1}$ cm$^{-2}$ sr$^{-1}$, for instance, probe the baryonic matter with $T = 10^6 - 10^{7.5}$ K and overdensity of $\rho/\bar{\rho} = 10^{0.5} - 10^2$ almost independently of the metallicity models. The Ovii 561eV emission lines, on the other hand, are sensitive to the WHIM with $T = 10^{6.5} - 10^{7.5}$K and $\rho/\bar{\rho} = 10 - 10^2$, relatively higher temperature and higher density regions than those probed by Oviii. In the temperature range of $T = 10^{6.5-7}$ K, the emissivity of Oviii is higher than that of Ovii. Thus one expects that when the Ovii triplet emission lines are detected, the corresponding Oviii emission line should also show up at the same redshift. Then one may estimate of the WHIM temperature using the line intensity ratios between Oviii and Ovii as long as the WHIM is well approximated as a single temperature structure. In reality, the WHIM over each smoothed region may be in a multi-temperature phase, and in this case the temperature estimation becomes more complicated since the Ovii emissivities have their peaks around $T = 2 \sim 3 \times 10^6$ K while the Oviii emissivity is larger than those of Ovii lines at $T > 3 \times 10^6$ K. Finally because of the rapid decrease of the emissivity of Ovii and Oviii below $10^6$ K, it is unlikely that one may detect WHIM with $T < 10^6$ K through the oxygen emission lines.

## 6.   Implications and discussion

In this paper, we have examined in detail the detectability of WHIM through Oviii and Ovii emission lines using a cosmological hydrodynamic simulation of intergalactic medium. Assuming a detector which has a large throughput $S_{\rm eff}\Omega = 10^2$ cm$^2$ deg$^2$ and a high energy

12

resolution $\Delta E = 2$ eV, we have presented simulated spectra of WHIM in the collisional ionization equilibrium at soft X-ray band $E = 500 - 700$ eV. Since the metallicity distribution in intergalactic space is quite uncertain, we adopted four simple and phenomenological models. In all the models we found that within the exposure time of $T_{\text{exp}} = 10^{5-6}$ sec our proposed detector can reliably identify OVIII emission lines of WHIM with $T = 10^{6-7}$ K and $\delta = 10^{0.5-2}$, and OVII emission lines of WHIM with $T = 10^{6.5-7}$ K and $\delta = 10^{1-2}$. The WHIM in these temperature and density ranges cannot be detected with the current X-ray observations except for the oxygen absorption features toward bright QSOs (e.g., Nicastro et al. 2002; Fang et al. 2002; Simcoe, Sargent, & Rauch 2002).

Let us remark three important issues related to the detectability of the WHIM. While they are beyond the scope of the present paper, we are currently working on those, and hope to report the results elsewhere in due course.

1. Our analysis has assumed that the WHIM is in the collisional ionization equilibrium. Strictly speaking, however, this assumption may not be justified in most regions of the WHIM, since the recombination time-scale is longer than the age of the universe. For example, in the region with $n_e = 10^{-5}$ cm$^{-3}$ and $T = 10^6$K, the recombination time-scale of HII is $3 \times 10^{11}$ yr, while the time-scale of the collisional ionization is much shorter $\simeq 10^5$ yr. Thus, WHIM is thought to be in over-ionized state, and emission lines can be produced by recombination and subsequent cascades in contrast to the collisional ionization equilibrium state. Unfortunately, it is not clear if the non-equilibrium effect increases or decreases our present estimate of the Oxygen line emission without accurate numerical calculation. Therefore, we plan to perform a proper treatment of the non-equilibrium ionization evolution to determine the line intensities of OVII and OVIII.

2. Furthermore Churazov et al. (2001) pointed out that the resonant line scattering of the CXB photons by OVIII and OVII ions can exceed the thermal emission in the relatively low-density WHIM with $\delta \simeq 10$ and $T \simeq 10^5 - 10^6$ K. Since the thermal emission lines that we computed mostly come from the higher density and higher temperature regions ($\delta \gtrsim 10^2$ and $T > 10^6$ K), the effect of the resonant line scattering may not be dominant. Nevertheless it should tend to increase the overall detectability of WHIM.

3. The ability of an unambiguous identification of OVII and OVIII lines in the observed spectra is an important issue that we have to address. If both OVIII and OVII lines at the same redshift are detected simultaneously, the identification is relatively easy. If one detects OVIII lines but no corresponding OVII counterparts, one has to worry about the possibility for other contaminating lines such as Fe XVII lines and OVIII Ly-$\beta$ line. If we have very hot ($> 10^7$K) at redshift $z > 0.1$, Fe XVII lines show up at $E < 650$eV and contaminate OVIII lines at low redshift. Actually, Figures 7 and 8 show emission lines of Fe XVII in our simulated spectra for some regions, which are significant contaminations against the proper identification of WHIM emission line systems. Another important issue

is how to estimate the temperature and density of the WHIM from the OVIII and OVII lines. These are crucial in discussing the cosmological implications of the WHIM signature from the given survey area.

Finally we would like to emphasize that a dedicated X-ray survey mission with the capabilities assumed in the present simulation is now under serious consideration. The size and mass of the satellite will be as small as $(1.5 \text{ m})^3$ and less than 300 kg. The scientific payloads will incorporate several advanced technologies that have been developed for the past and future Japanese X-ray astronomy missions. The basic structure of the X-ray telescope is a thin-foil multi-mirror type already used for ASCA and Astro – E II. The major innovation in the design optimized for the dedicated WHIM survey is the use of 4 reflection telescope, i.e., X-rays are reflected by 4 conical-shape mirrors. This technique achieves a substantial reduction of the focal length down to 60–70 cm, by a factor of $\gtrsim 6$ relative to that of the 2 reflection type. Thus the extremely compact satellite becomes possible. A preliminary study shows that our requirement, $S\Omega \gtrsim 100 \text{ cm}^2\text{deg}^2$, can be achieved in the energy band 0.5–0.7 keV with the mirror outer diameter of 36 cm. The focal plane instrument will be an array of TES micro-calorimeters, cooled by mechanical coolers and adiabatic demagnetization refrigerators. The energy resolution is 2 eV and the sensitive area of the detector is about 1.5 cm $\times$1.5 cm consisting of even up to 1024 pixels. Such a detector can cover $1° \times 1°$ field if the focal length is less than 86 cm. The current status of the detector development will be reported elsewhere. We expect that within 2–3 yrs the required techniques for the survey of WHIM will be quite feasible, and hope that the small satellite will be launched before 2010.

## References

Aguirre, A., Hernquist, L., Katz, N., Gardner, J., & Weinberg, D.H. 2001, ApJ, 556, L11

Aguirre, A., Hernquist, L., Schaye, J., Katz, N., Weinberg, D.H., & Gardner, J. 2001, ApJ, 561, 521

Burles, S., & Tytler, D. 1998, ApJ, 507, 732

Cen, R. & Ostriker, J. 1999a, ApJ, 514, 1

Cen, R. & Ostriker, J. 1999b, ApJ, 519, L109

Cen, R., Tripp, T.M., Ostriker, J.P., & Jenkins, E.B. 2001, ApJ, 559, 5

Churazov, E., Haehenelt, M., Kotov, O., & Sunyaev, R. 2001, MNRAS, 323, 93

Croft, R.A.C., Di Matteo, T., Davé, R., Hernquist, L., Katz, N., Fardal, M.A., & Weinberg, D.H. 2001, ApJ, 557, 67

Davé, R., Cen, R., Ostriker, J.P., Bryan, G.L., Hernquist, L., Katz, N., Weinberg, D.H., Norman, M.L., & O'Shea, B. 2001, ApJ, 552, 473

Fang, T., & Canizares, C.R. 2000, ApJ, 532, 539

Fang, T., & Bryan, G.L. 2001, ApJ, 561, L31

Fang, T., Bryan, G.L., & Canizares, C.R. 2002, 564, 604

Fang, T., Marshall, H.L., Lee, J.C., Davis, D.S., & Canizares, C.R., 2002, ApJ, 572, L127

Ferrara, A., Pettini, M., & Shchekinov, Y. 2000, MNRAS, 319, 539

Fukugita, M., Hogan, C.J., & Peebles, P.J.E. 1998, ApJ, 503, 518

Gnedin, N.Y. & Ostriker, J.P. 1997, ApJ, 486, 581

Gnedin, N.Y. 1998, MNRAS, 297, 407

Hellsten, U., Gnedin, N.Y., & Miralda-Escude, J. 1998, ApJ, 509, 56

Kaastra, J.S., Lieu, R., Tamura, T., Paerels, F.B.S., & den Herder, J.W. 2003, A&A, 397, 445

Kushino, A., Ishisaki, Y., Morita, U., Yamasaki, N.Y., Ishida, M., Ohashi, T., & Ueda, Y. 2002, PASJ, 54, 327

McCammon, D. et al. 2002, ApJ, 576, 188

Morrison R. & McCammon D., 1983, ApJ, 270, 119

Mewe, R., Gronenschild, E.H.B.M., & van den Oord, G.H.J., 1985, A&A S, 62. 197

Miyaji, T., Ishisaki, Y., Ogasaka, Y., Ueda, Y., Freyberg, M. J., Hasinger, G., & Tanaka, Y. 1998, A&A, 334, 13

Nath, B.B., & Trentham, N. 1997, MNRAS, 291, 505

Nicastro, F., Zezas, A., Drake, J., Elvis, M., Fiore, F., Fruscione, A., Marengo, M., Mathur, S., & Bianchi, S. 2002, ApJ, 573, 157

Perna, R., & Loeb, A. 1998, 503, L135

Phillips, L.A., Ostriker, J.P., & Cen, R. 2001, ApJ, 554, 9

Simcoe, R.A., Sargent, W.W., & Rauch, M. 2002, ApJ, 578, 737

Strüdel L., et al. 2001, A&A, 365, L18

Sutherland, R.S., & Dopita, M.A. 1993, ApJS, 88, 253

Tripp, T.M., Savage, B.D., & Jenkins, E.B. 2000, ApJ, 534, L1

Tripp, T.M., Giroux, M.L., Stocke, J.T., Tumlinson, J. & Oegerle, W.R. 2001, ApJ, 563, 724

Weisskopf, M., Tananbaum, H., Van Speybroeck, L., & O'Dell,S., 2000, Proc. SPIE, 4012, 2

Yoshikawa, K., Taruya, A., Jing, Y.P., & Suto, Y. 2001, ApJ, 558, 520

**Table 1.** Specification and Detection limit of emission lines for various future and current X-ray satellites.

| satellite | year | $S_{\mathrm{eff}}$ [cm$^2$] | $S_{\mathrm{eff}}\Omega$ [cm$^2$deg$^2$] | $\Delta E$ [eV] | $f_{\mathrm{lim}}$ [erg/s/cm$^2$/sr] |
|---|---|---|---|---|---|
| Chandra ACIS-S3 | 1999 | 600 | 12 | 80 | $10^{-9}$ |
| XMM-Newton EPIC-pn | 1999 | 1200 | 100 | 80 | $3 \times 10^{-10}$ |
| Astro-E II XIS | 2005 | 90×4 | 36 | 80 | $6 \times 10^{-10}$ |
| Astro-E II XRS | 2005 | 90 | 0.23 | 6 | $2 \times 10^{-8}$ |
| Const-X SXT+TES | mid-2010's | 3000 | 5.6 | 2 | $7 \times 10^{-10}$ |
| XEUS-I | mid-2010's | 60000 | 16.7 | 2 | $2.5 \times 10^{-10}$ |
| our model detector | $\sim 2010$ | (100∼200) | 100 | 2 | $6 \times 10^{-11}$ |
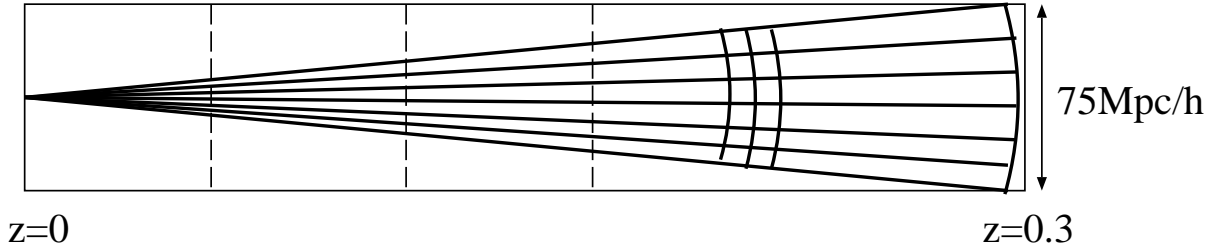


**Fig. 1.** A schematic picture of our lightcone output in the comoving coordinate. The eleven cubic simulation data are stacked along the line of sight up to $z=0.3$ as described in the text. The surface brightness are computed on $64 \times 64$ grids over the $5° \times 5°$ celestial area. Thus the angular size of the simulated grid is $5°/64 = 4.7$ arcmin.
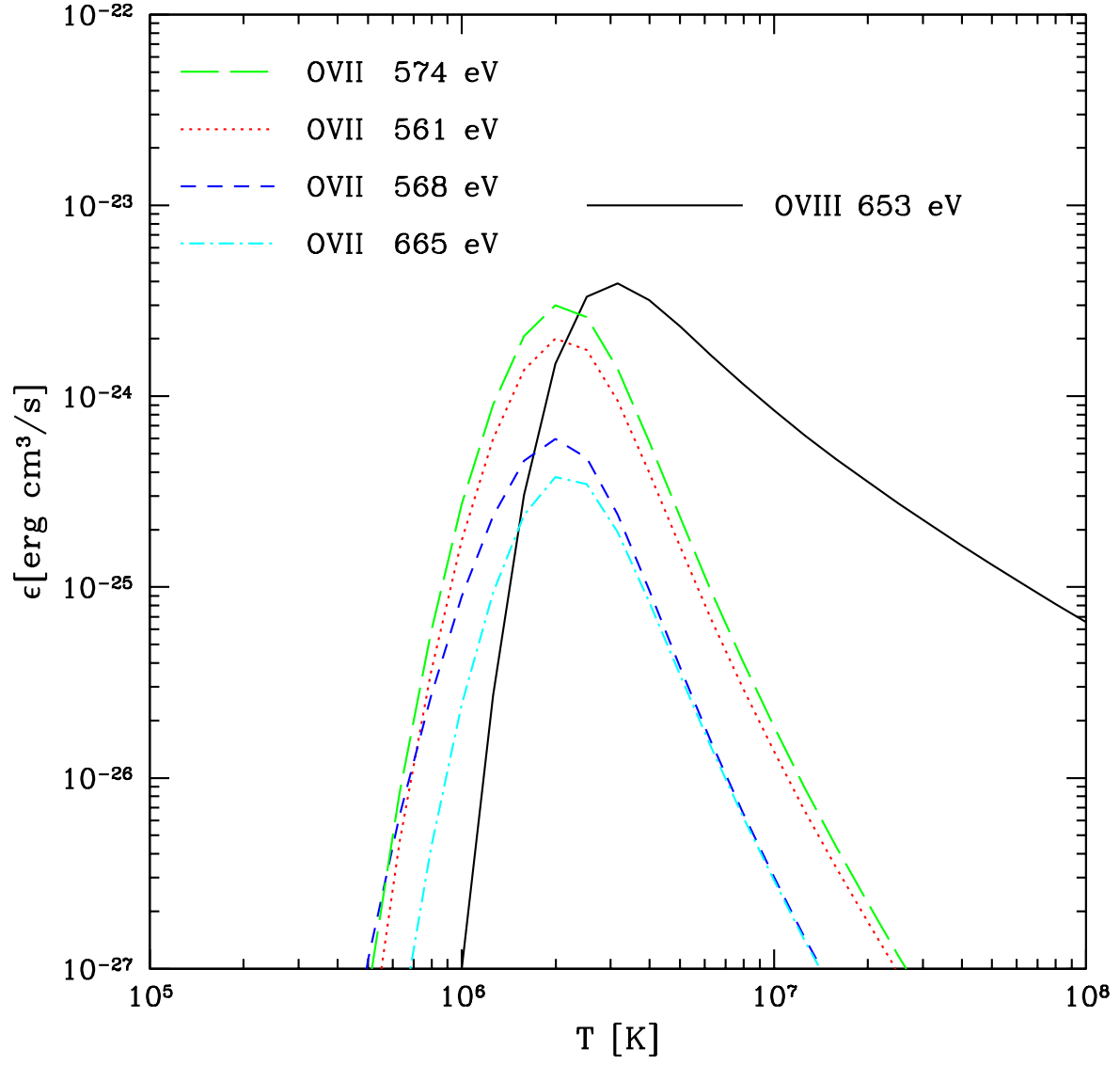
**Fig. 2.** Emissivity of OVII and OVIII lines in collisional ionization equilibrium.

17
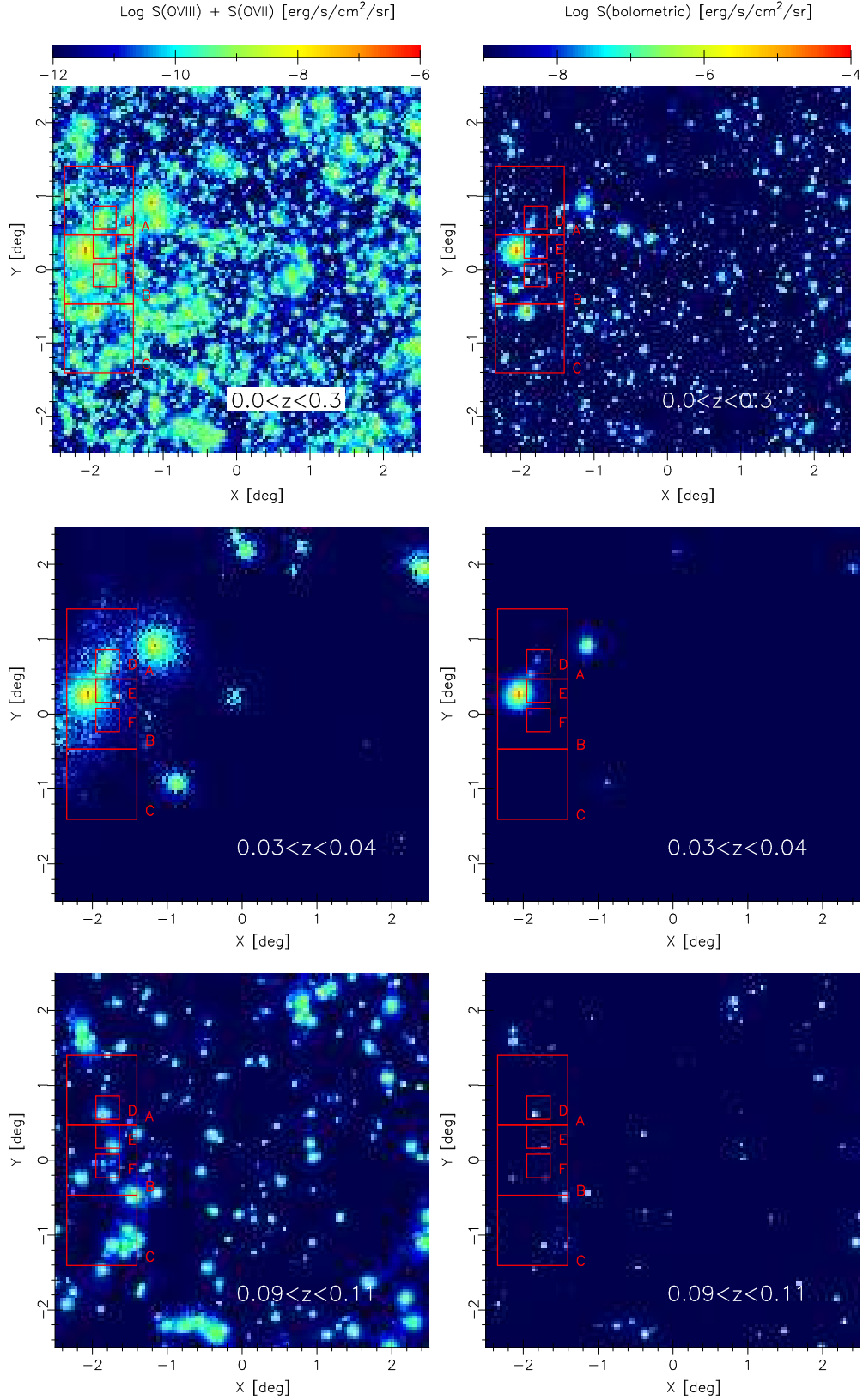
**Fig. 3.** The map of OVIII and OVII emission (*left panels*) and X-ray bolometric emission (*right panels*) from $0.0 < z < 0.3$ (*upper panels*), from $0.03 < z < 0.04$ (*middle panels*), and from $0.09 < z < 0.11$ (*lower panels*). Squares indicate regions of which the simulated spectra in Figure 7 and 8 are calculated.
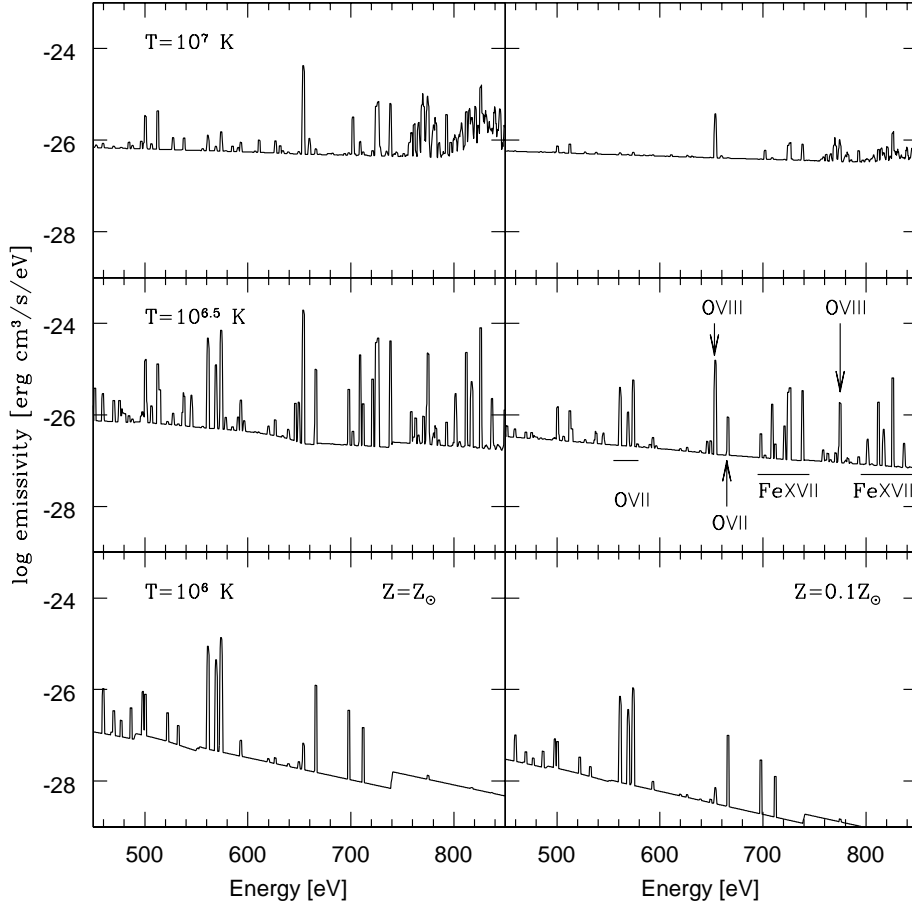
**Fig. 4.** Template spectra of collisionally ionized plasma with temperature $T = 10^6$ K (*lower panels*), $10^{6.5}$ K (*middle panels*), and $10^7$ K (*upper panels*). Spectra for metallicity $Z = Z_\odot$ and $Z = 0.1 Z_\odot$ are shown in the left and right panels, respectively.
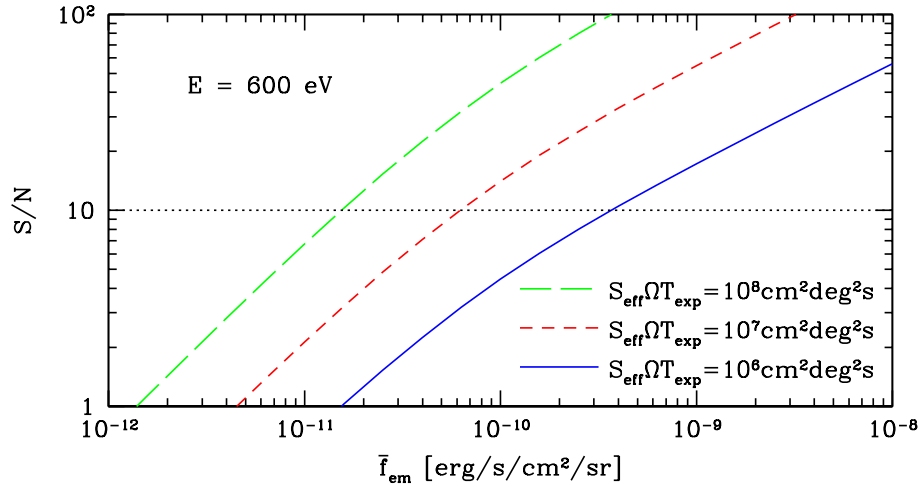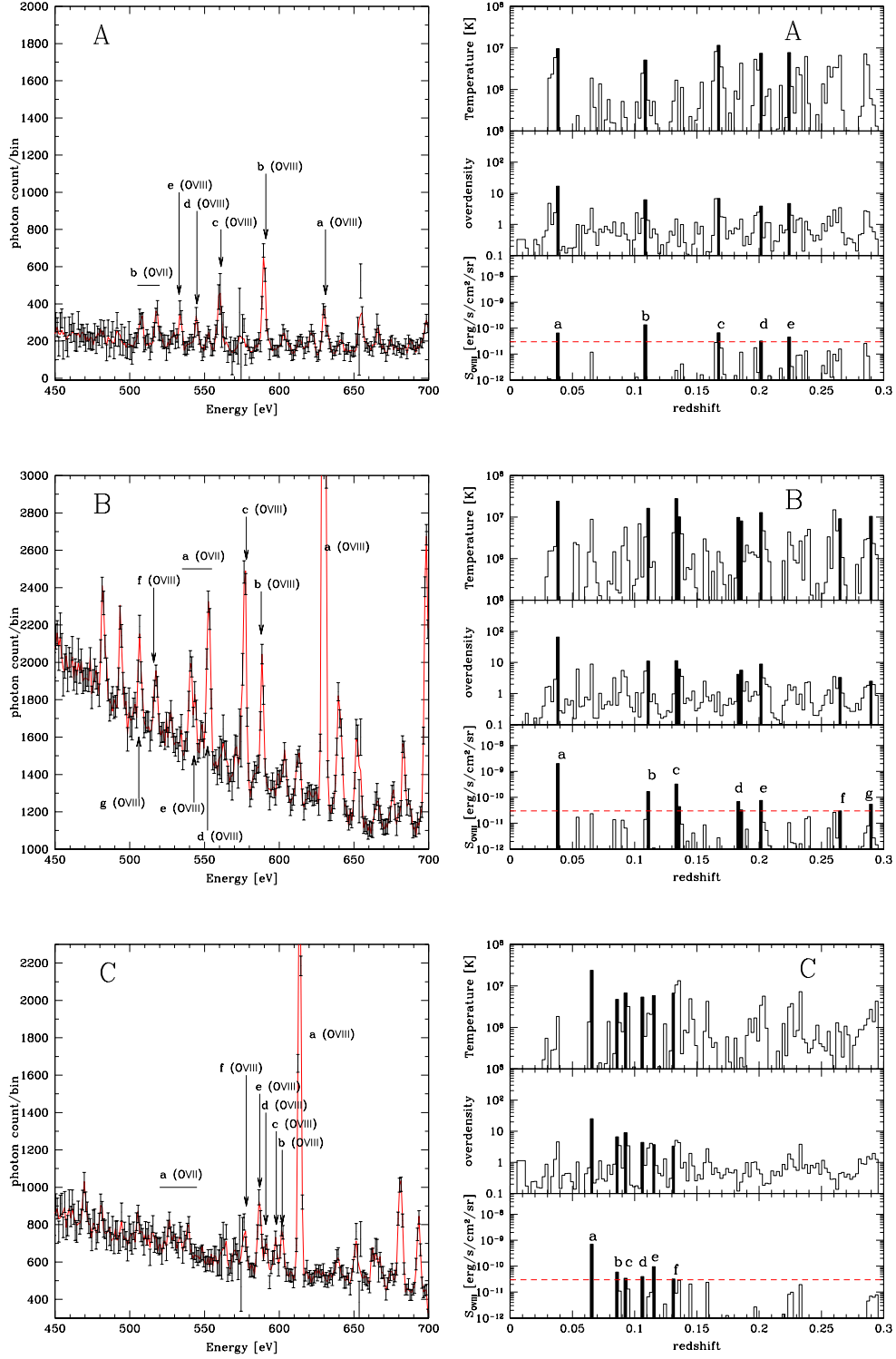


**Fig. 5.** Signal-to-Noise ratio of OVIII emission lines embedded in the CXB for various values of $S_{\text{eff}} \Omega T_{\text{exp}}$.
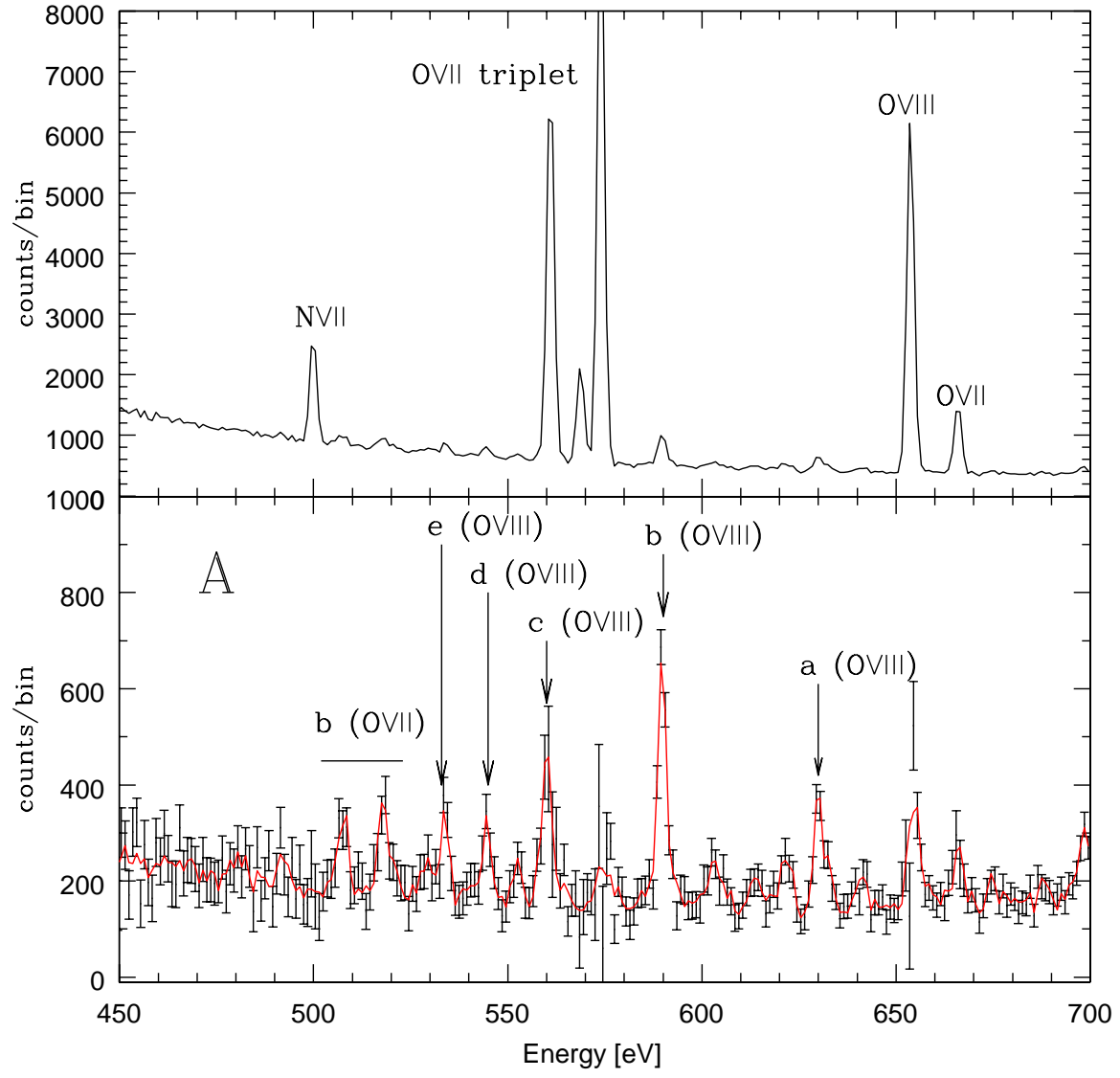
**Fig. 6.** A simulated spectrum along a line of sight. *Upper panel* shows emission lines of WHIM, the CXB and the Galactic emission. *Lower panel*: The spectrum of WHIM after the CXB and the Galactic emission are subtracted. The metallicity model I is adopted.
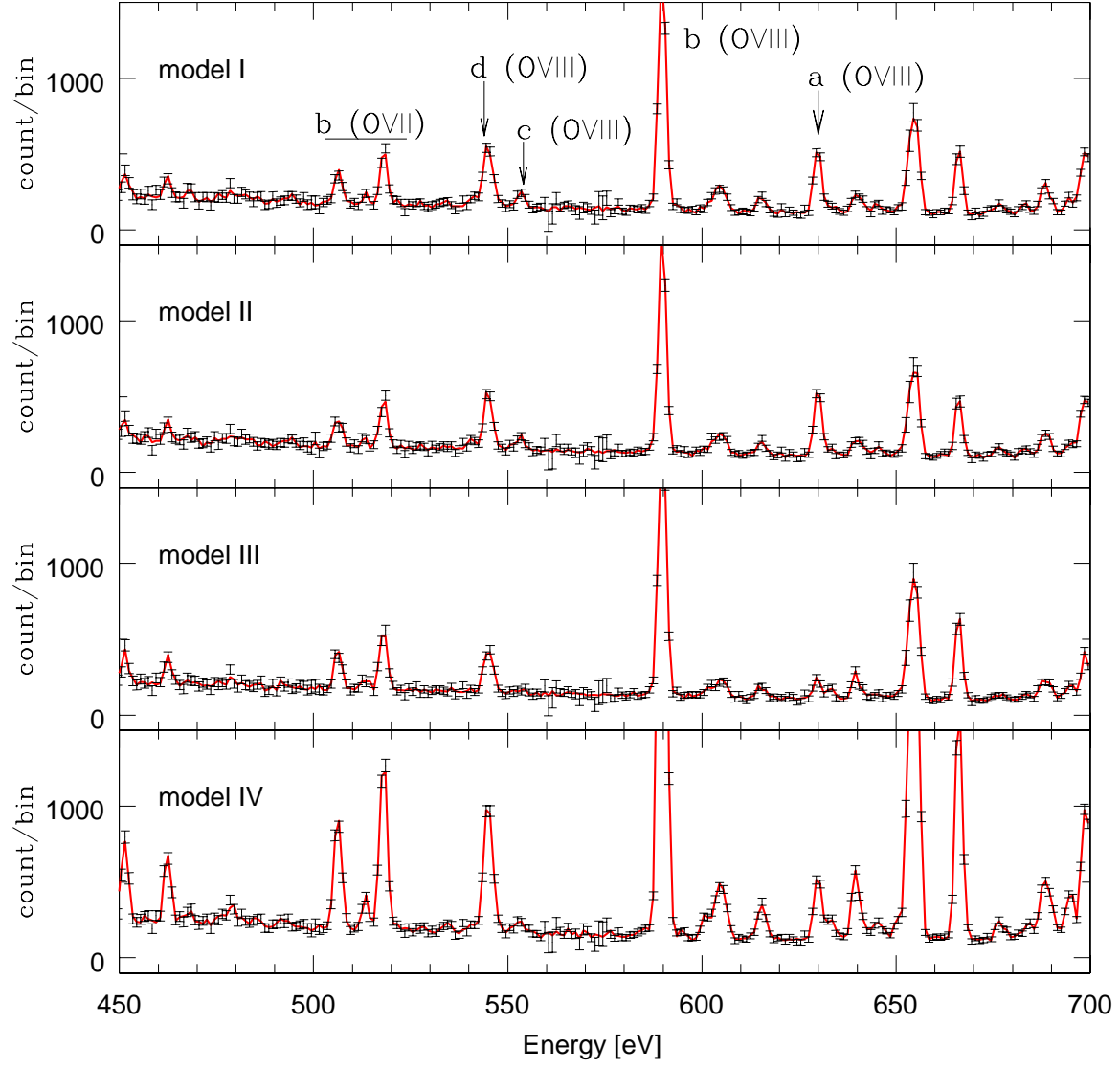
**Fig. 7.** The simulated spectra and redshift profiles of gas density, temperature and OVIII surface brightness along the three line-of-sights marked in Figure 3, A (*upper*), B (*middle*), C (*lower*).
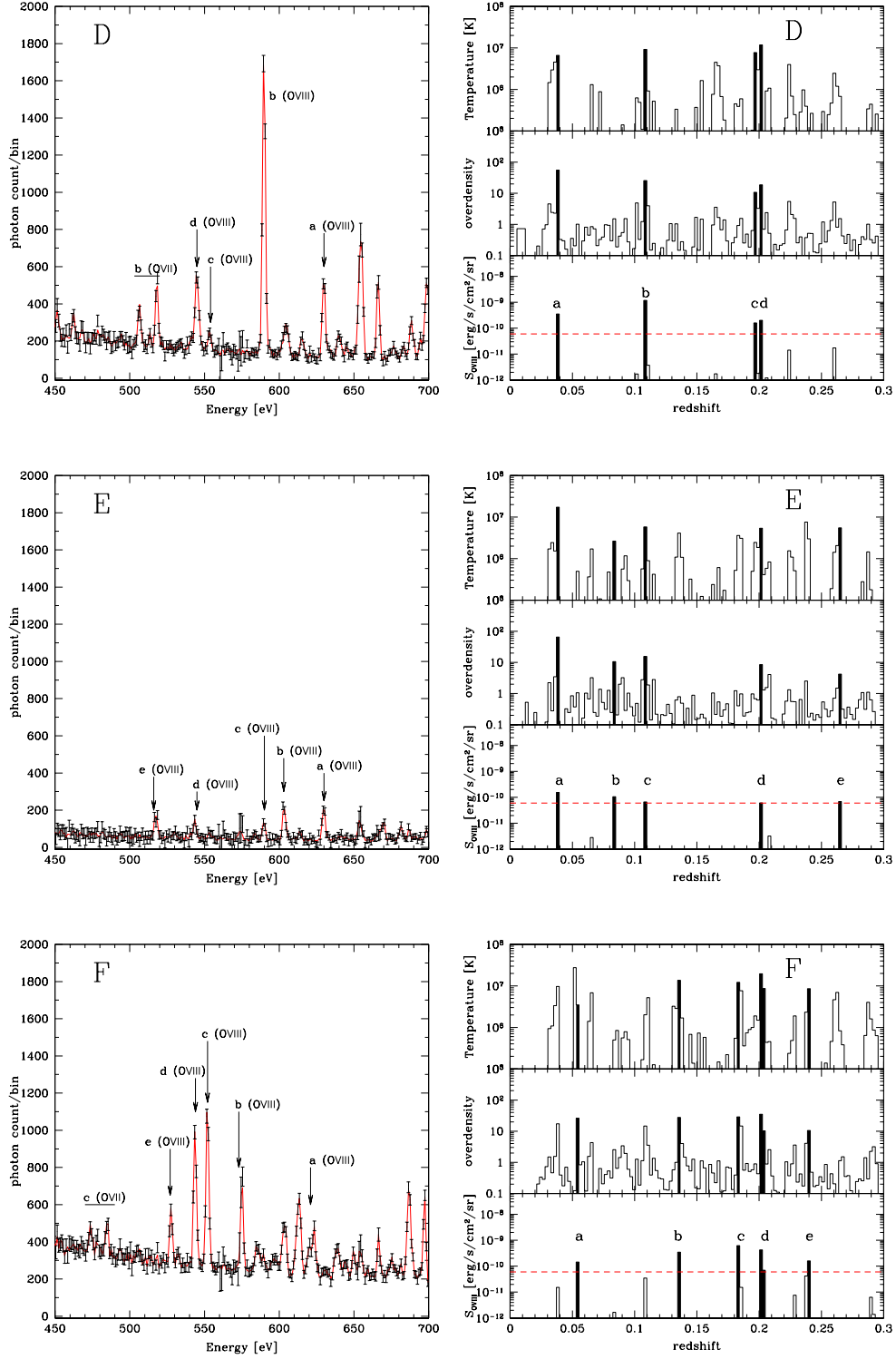
**Fig. 8.** The simulated spectra and redshift profiles of gas density, temperature and OVIII surface brightness along the three line-of-sights marked in Figure 3, D (*upper*), E (*middle*), F (*lower*).

**Fig. 9.** The simulated spectra along the region D for the four metallicity models.
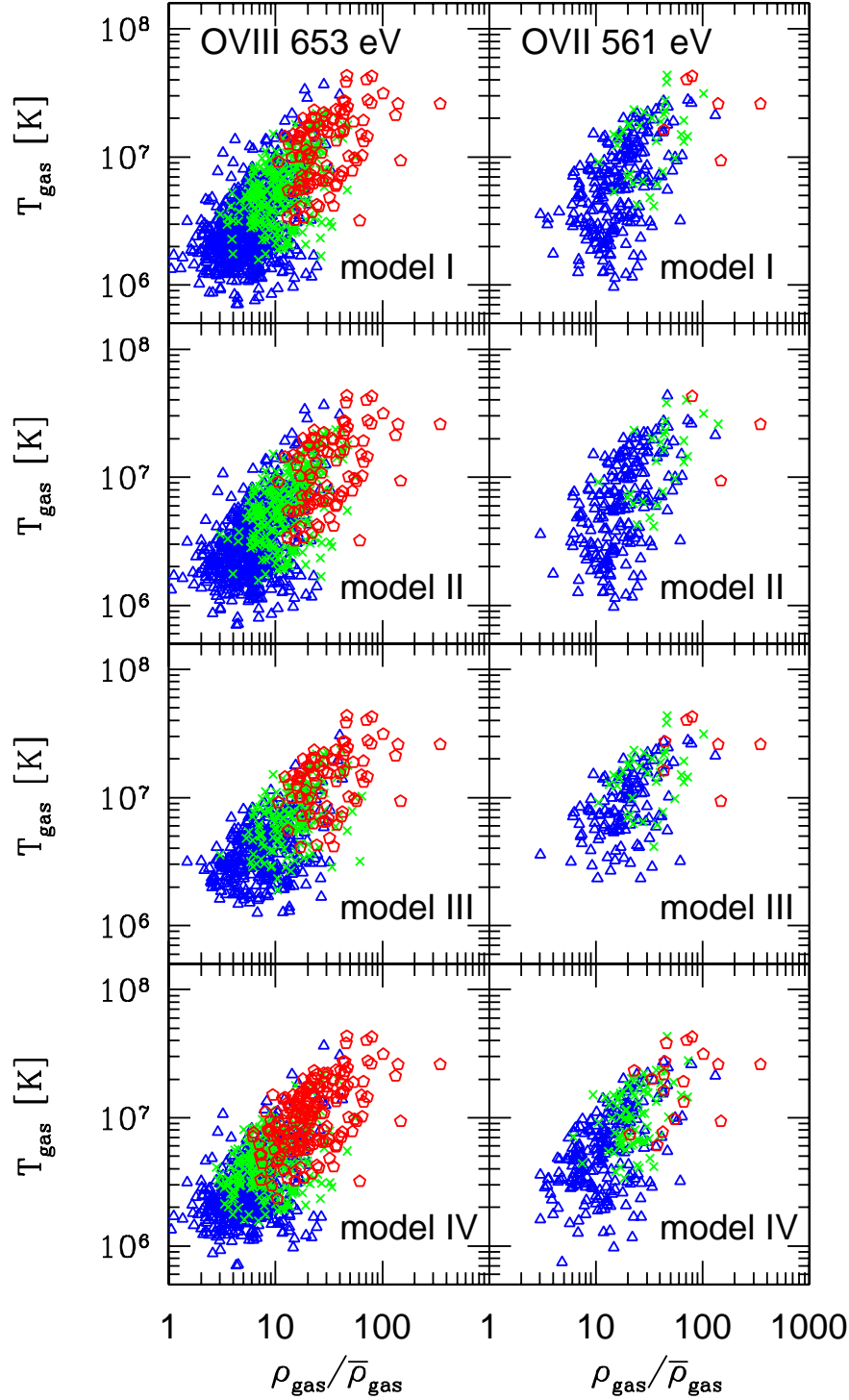
**Fig. 10.** The distribution of baryons on the $\rho/\bar{\rho}$–$T$ plane for the four metallicity models. Different symbols indicate the three ranges of surface brightness of the emission lines; Red pentagons, green crosses and blue triangles correspond to regions with surface brightness $S[\mathrm{erg/s/cm^2/sr}] > 3 \times 10^{-10}$, $3 \times 10^{-10} > S[\mathrm{erg/s/cm^2/sr}] > 6 \times 10^{-11}$ and $6 \times 10^{-11} > S[\mathrm{erg/s/cm^2/sr}] > 10^{-11}$, respectively, for the OVIII 653eV (*left panels*) and OVII (*right panels*) line emissions.